Research Article

Artyom Assadillayev, Tatsuki Hinamoto, Minoru Fujii, Hiroshi Sugimoto and Søren Raza*

Thermal near-field tuning of silicon Mie nanoparticles

https://doi.org/10.1515/nanoph-2021-0424
Received August 3, 2021; accepted September 19, 2021;
published online October 4, 2021

Abstract: Tunable high-refractive-index nanostructures are highly desired for realizing photonic devices with a compact footprint. By harnessing the large thermo-optic effect in silicon, we show reversible and wide thermal tuning of both the far- and near-fields of Mie resonances in isolated silicon nanospheres in the visible range. We perform *in situ* heating in a transmission electron microscope and electron energy-loss spectroscopy to show that the Mie resonances exhibit large spectral shifts upon heating. We leverage the spectral shifts to demonstrate near-field tuning between different Mie resonances. By combining electron energy-loss spectroscopy with energy-dispersive X-ray analysis, we show a reversible and stable operation of single silicon nanospheres up to a temperature of 1073 K. Our results demonstrate that thermal actuation offers dynamic near-field tuning of Mie resonances, which may open up applications in tunable nonlinear optics, Raman scattering, and light emission.

Keywords: electron energy-loss spectroscopy; high-refractive-index nanostructures; Mie resonances; near-field tuning; thermo-optic tuning.

***Corresponding author**: **Søren Raza**, Department of Physics, Technical University of Denmark, Fysikvej, DK-2800 Kongens Lyngby, Denmark, E-mail: sraz@dtu.dk. https://orcid.org/0000-0002-0296-7202
Artyom Assadillayev, Department of Physics, Technical University of Denmark, Fysikvej, DK-2800 Kongens Lyngby, Denmark, E-mail: artas@dtu.dk. https://orcid.org/0000-0002-5117-2748
Tatsuki Hinamoto, **Minoru Fujii and Hiroshi Sugimoto**, Department of Electrical and Electronic Engineering, Kobe University, Rokkodai, Nada, Kobe 657-8501, Japan, E-mail: tatsuki.hinamoto@gmail.com (T. Hinamoto), fujii@eedept.kobe-u.ac.jp (M. Fujii), sugimoto@eedept.kobe-u.ac.jp (H. Sugimoto). https://orcid.org/0000-0001-6607-2574 (T. Hinamoto)

1 Introduction

Dielectric and semiconductor nanostructures are rapidly becoming one of the main constituents in nanoscale optical devices. Due to their high refractive index and low nonradiative losses, they support magnetic and electric multipole Mie resonances on subwavelength scales [1]. Dielectric nanoparticles have been exploited for a number of applications, such as dielectric nanoantennas [2–5], resonant nonlinear optics [6–8], and metasurfaces [9–12]. In most cases, nanoresonators or metasurfaces are operated statically, i.e., the optical response of the system is fixed upon fabrication. However, many applications require tunable optical elements, where the optical response can be controlled with an external stimulus [13, 14]. This has prompted a strong interest in realizing dielectric optical components with a tunable far-field functionality and has led to the successful demonstrations of different tuning mechanisms, including photothermal [15, 16], electromechanical [17, 18], via photocarrier generation [19, 20], coupling to liquid crystals [21–23], using phase change materials [24–26], and through the thermo-optic effect [27, 28]. In this regard, the thermo-optic effect, i.e., the change in the refractive index n with temperature T, is an appealing tuning mechanism as it provides reversible, continuous and large spectral shifts of optical Mie resonances by simply tuning the temperature. Recent work has demonstrated that it is possible to thermally tune the far-field optical response of nanoparticles and metasurfaces made of silicon, germanium, lead telluride [27, 29–32], and hybrid silicon–gold [33]. Silicon is particularly interesting for dynamic thermal tuning due to its combination of high refractive index, complementary metal-oxide-semiconductor (CMOS) compatibility, and high thermo-optic coefficient $\mathrm{d}n/\mathrm{d}T$ [31]. However, thermal tuning of silicon has so far been limited to nano- and micron-sized structures with resonances in the infrared spectral ranges, where a modest tunability of Mie resonances is observed. Shifting the resonances into the visible is expected to increase the tuning range due to an increased thermo-optic coefficient near the direct bandgap edge of silicon. In

addition, tunable dielectric components have been heavily focused on far-field functionalities with little attention devoted to the near-field. Yet, many important optical processes rely on the properties and enhancement of the near-field, such as nonlinear processes [8, 34], Raman scattering [35–37], and light emission [38–40], and, as such, dynamic tuning of the near-field in high-index nanostructures could open up for new applications in these areas.

Here, we demonstrate reversible and wide thermal tuning of both the far- and near-fields of Mie resonances in isolated silicon nanoparticles in the visible range. We perform *in situ* heating with temperatures reaching 1073 K in a scanning transmission electron microscope (STEM) and map the spatial and spectral changes of the Mie resonances using electron energy loss spectroscopy (EELS). The extreme spatial resolution of EELS along with its capability to characterize both the near- and far-field optical response [41–43] have been exploited to study a variety of optical nanostructures [44–48] and recently also nanodevices [49]. Using *in situ* EELS, we show that the Mie resonances exhibit large spectral shifts upon heating and that the near-field can be dramatically altered at fixed energies. In particular, we show that we can tune between the near-fields of different Mie resonances. Furthermore, we extend our EELS and STEM measurements with energy-dispersive X-ray (EDX) analysis, which allows us to correlate structural and chemical changes to the near- and far-field optical response. We find that the silicon nanoparticles can be repeatedly heated to temperatures up to 1073 K without any structural, chemical, or optical degradation. Our *in situ* EELS results provide a unique insight into thermal-induced near-field tuning at the scale of individual silicon Mie nanoparticles.

2 Results

2.1 Thermal tuning of Mie resonances

Crystalline silicon nanoparticles with a spherical shape are prepared in a colloidal suspension [5] and deposited on top of commercially available TEM chips [48], which use ceramic elements for heating. Figure 1(a) shows a

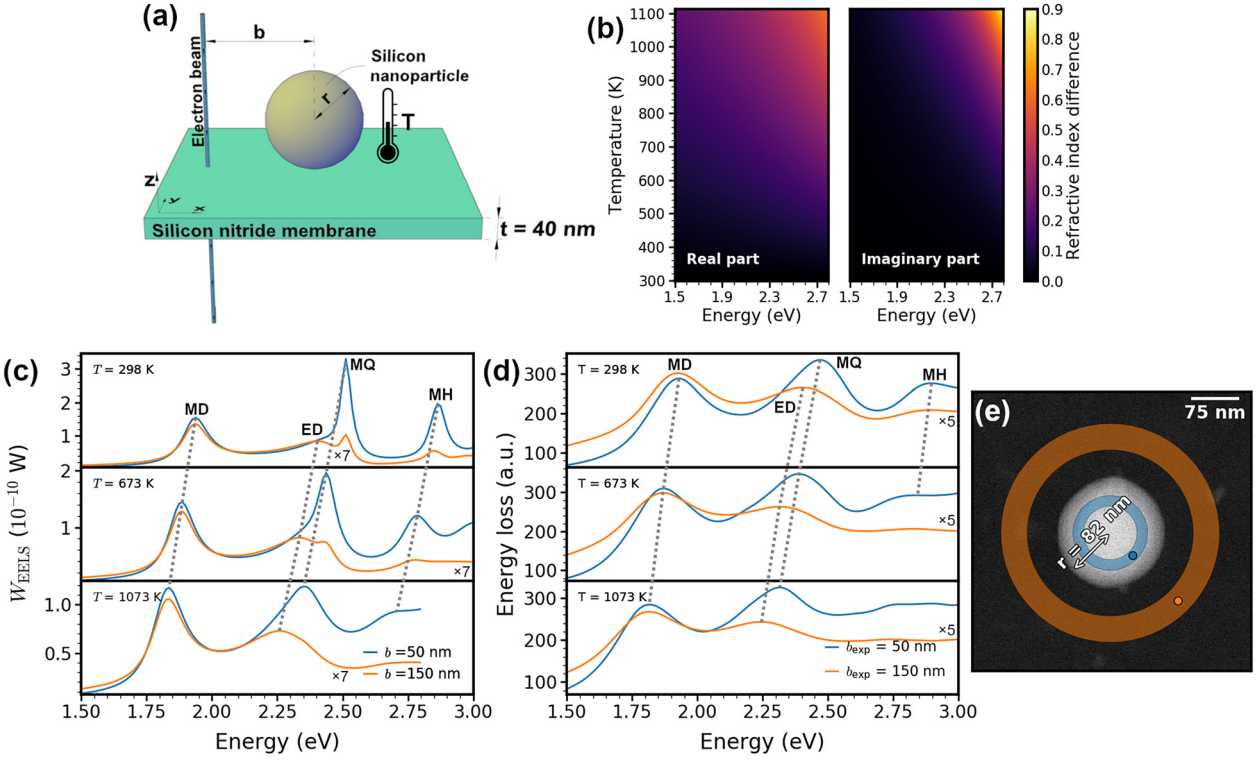

Figure 1: Thermal tuning of Mie resonances in silicon nanoparticles. (a) Schematic of a silicon nanoparticle of radius r placed on a silicon nitride membrane and excited by an electron beam. The impact parameter b denotes the distance between the electron beam and the center of the nanoparticle. The temperature is applied to the nanoparticle by a ceramic heater located around the nitride membrane. (b) Temperature modulation of the refractive index of silicon. (c) Simulated and (d) experimental EELS spectra of a silicon nanoparticle with a radius $r = 82.4 \pm 1.9$ nm acquired from the electron beam positions shown in (e). (e) STEM image of the nanoparticle, where the colored areas represent the integration regions for the experimental EELS signal, and the colored points are the position of the electron beam in the simulation.

schematic of the resulting structure, where an isolated silicon nanoparticle is on top of a silicon nitride membrane. The ceramic heater is located several micrometers from the nanoparticle (not shown). Upon heating, the refractive index of silicon is modified due to the thermo-optic effect (Figure 1(b)). Silicon has a positive thermo-optic coefficient in the energy region from 1.5 to 3 eV due to the temperature-induced changes in the electronic transitions in silicon [50], which leads to an increase of the real part of the refractive index by up to 0.6 at 1100 K in comparison to room temperature. Silicon also exhibits a negative thermo-optic coefficient for energies higher than the temperature-dependent direct bandgap edge (3.4 eV at room temperature [51]), or a nonnegligible concentration of thermally-generated free carriers [30]. Figure 1(b) also shows the increase in the imaginary part of the refractive index that is mainly due to increased phonon population at elevated temperatures, which results in an increase in the probability of indirect transitions and, hence, to increased light absorption [52]. This effect is most pronounced in the violet part of the spectrum since this is close to the direct bandgap energy of silicon.

We perform EELS characterization both via simulation and experiment of a silicon nanoparticle with a radius $r = 82.4 \pm 1.9$ nm (Figure 1(c) and (d)). The electron beam excites the nanoparticle at the positions indicated in Figure 1(e). These positions are selected based on the fact that the electric dipole (ED) has a larger EELS response outside the particle, while the magnetic quadrupole (MQ) and magnetic hexapole (MH) are predominantly excited inside the particle, halfway to the edge [48]. We observe redshifts of all Mie modes (magnetic dipole (MD), ED, and MQ) in the silicon nanoparticle in both experiment and simulation with increasing temperature. The redshift is due to the increasing real part of the refractive index at elevated temperatures. The MD resonance energy is shifted by 0.1 eV as the temperature is elevated to 1073 K, while the higher-order ED, MQ, and MH modes show larger shifts of around 0.15 eV each. The electric quadrupole (EQ), which is predominantly excited in the middle of the particle [48], has a comparable shift of 0.15 eV (see Supplementary Figure S1). In addition, the thermally-induced increase in the imaginary part of the refractive index of silicon near the direct bandgap edge leads to a significant broadening of the MH mode. Combined with the spectral resolution of the EELS setup, it is not possible to safely identify the MH mode at temperatures above 673 K. The EQ mode behaves similarly (see Supplementary Figure S1).

The analysis of the thermal tuning of Mie resonances is further extended to various particle sizes in Figure 2(a). The

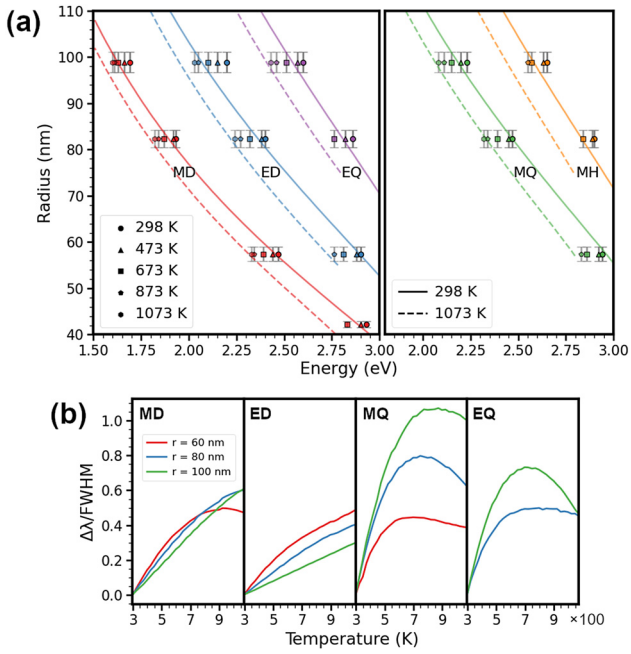

Figure 2: Tunability of Mie resonances. (a) Measured resonance energies as a function of particle radius and temperature for the first five Mie resonances in silicon nanoparticles. The color points represent experimental values, and the color lines show the first maxima of the different Mie scattering coefficients. ED/EQ and MQ/MH resonances are separated into two plots for clarity. (b) Simulated linewidth tunability as a function of temperature for the first four Mie modes supported by silicon nanoparticles with different radii.

change in the first five Mie mode (MD, ED, MQ, EQ, and MH) resonance energies of the nanoparticles with 40–100 nm radii are analyzed experimentally and compared to theoretical predictions. The close match between the theory and experiment for broad nanoparticles size range shows the possibility to thermally tune all nanoparticle Mie modes by up to 0.15 eV when the temperature is increased to 1073 K. The modes which are closer to the red side of the spectrum experience the lower shift of around 0.1 eV. Different spectral shifts as a function of resonances excited are due to nonlinear dependence of the refractive index with energy and temperature. From Figure 1(b), it can be seen that there is a larger change in the real part of the refractive index in comparison to the room temperature at higher energies. This leads to larger spectral shifts at higher energies; consequently, Mie modes with higher resonance energy (e.g., higher-order modes) experience larger spectral shifts.

Due to the mode broadening caused by the increase in the imaginary part of the refractive index and the energy resolution of our EELS setup, some Mie modes located above 2.5 eV at high temperatures cannot be experimentally resolved. In particular, at temperatures above 673 K,

the MD mode disappears for the smallest particle (42 nm radius), the MH and EQ resonances disappear in the middle nanoparticle size region (82 nm radius), while larger particles (99 nm radius) are not affected.

The thermal tunability of the Mie resonances depends on their resonance energy (defined by the particle size) since resonance energies close to the direct bandgap energy of silicon will be subject to both large refractive index changes and increased optical losses at elevated temperatures. In the following, we quantify this effect by using linewidth tunability as a measure for the thermal tunability of the Mie resonances. The linewidth tunability is defined as the spectral shift of the Mie resonance energy at elevated temperatures relative to the room temperature, normalized by the resonance full-width at half-maximum at the elevated temperature (see Methods). A linewidth tunability above one, therefore, corresponds to tuning the resonance energy more than one linewidth. We numerically show the linewidth tunability of the first four Mie modes supported by silicon nanospheres in the 60–100 nm radii range (Figure 2(b)). The MD mode shows a continuous increase by up to 0.6 tuning with the exception of the 60 nm particle, which peaks at 923 K and shows a slight decrease. The ED follows a similar increase trend with larger particles having smaller overall tunability. The higher-order MQ mode shows the largest linewidth tunability, reaching its maximal value at a higher temperature when the particle size is increased (700 K and 0.44 tuning for 60 nm particle, 820 K and 1.07 tuning for 100 nm particle). Increasing the temperature even further leads to a drop in the linewidth tunability due to thermally-induced broadening of the direct bandgap edge in silicon. The EQ tuning shows a similar lineshape with the peak value being approximately 1.5 times smaller. These results demonstrate that even fundamental Mie resonances can be optimized to achieve large thermal tunability with linewidth tunabilities reaching above unity.

2.2 Thermal near-field tuning of silicon Mie modes

A unique feature of *in situ* EELS is that it allows us to track the near-field changes in the EELS maps of the silicon nanoparticles with temperature. Using the characteristic EELS maps for different Mie modes at elevated temperatures (see Supplementary Figure S2), we demonstrate significant tuning of the near-field profiles at an energy of interest. We consider two cases of thermal near-field tuning for two different particle sizes. For a silicon particle with radius $r = 80$ nm, a multipole decomposition of the EELS spectrum [53] reveals that the main spectral contributions come from the two first azimuthal components $l = 1$ and $l = 2$ (Figure 3(a)). It is worth noting that $l = 1$ ($l = 2$) contains the resonant features of both the MD and ED (MQ and EQ). We fix the energy of interest at 2.4 eV which is the ED resonance energy at room temperature. By increasing the temperature to 1073 K, we can see from the multipole decomposition that the energy crosses the MQ peak. This is accompanied by significant changes in the experimental EELS maps presented in Figure 2(b) and (d). Indeed, we observe that the near field is tuned from the ED mode (at room temperature) to the MQ mode at $T = 1073$ K (see also Supplementary Figure S2 for characteristic maps).

We also perform a multipole decomposition of the EELS spectrum for a smaller nanoparticle with radius $r = 40$ nm in Figure 3(e). For this particle size, the EELS spectrum is dominated by the $l = 1$ contribution at both room temperature and $T = 1073$ K. We fix the energy of interest at 2.91 eV which is the MD resonance energy at the room temperature. By elevating the temperature to 1073 K, the energy of interest is now located in the flat region of the spectrum. Despite no observable peak from the ED in the EELS spectrum, we still observe experimentally that the near field dramatically changes from the MD mode to that characteristic of the ED mode as the temperature is elevated (Figure 3(f)–(h)). Importantly, this serves to show that near-field tuning remains accessible despite weak or lacking spectral features.

2.3 Stability

In situ EELS allows us to track morphological changes of the nanoparticles at elevated temperatures. These changes can be attributed to the possible changes in the nanoparticle size and geometry due to temperature, such as nanoparticle melting. This, combined with the EELS data, can be used to ensure a stable and reversible operation of the silicon nanoparticles when exposed to high temperatures.

We track the changes in the nanoparticle shape and size in Figure 4(a)–(d). The STEM images are taken at time gaps of several minutes between each other to ensure the thermally stable condition of the TEM chip. By careful image analysis, we determine the radius of the particle at different temperatures and find that the particle radius does not change for temperatures up to 1073 K. This demonstrates that there is no observable thermal expansion of the silicon nanoparticle. When the particle temperature increases beyond 1073 K we observe that the particle reshapes and becomes faceted (see Figure 4(d)). We extend this procedure to 31 different nanoparticles of various sizes

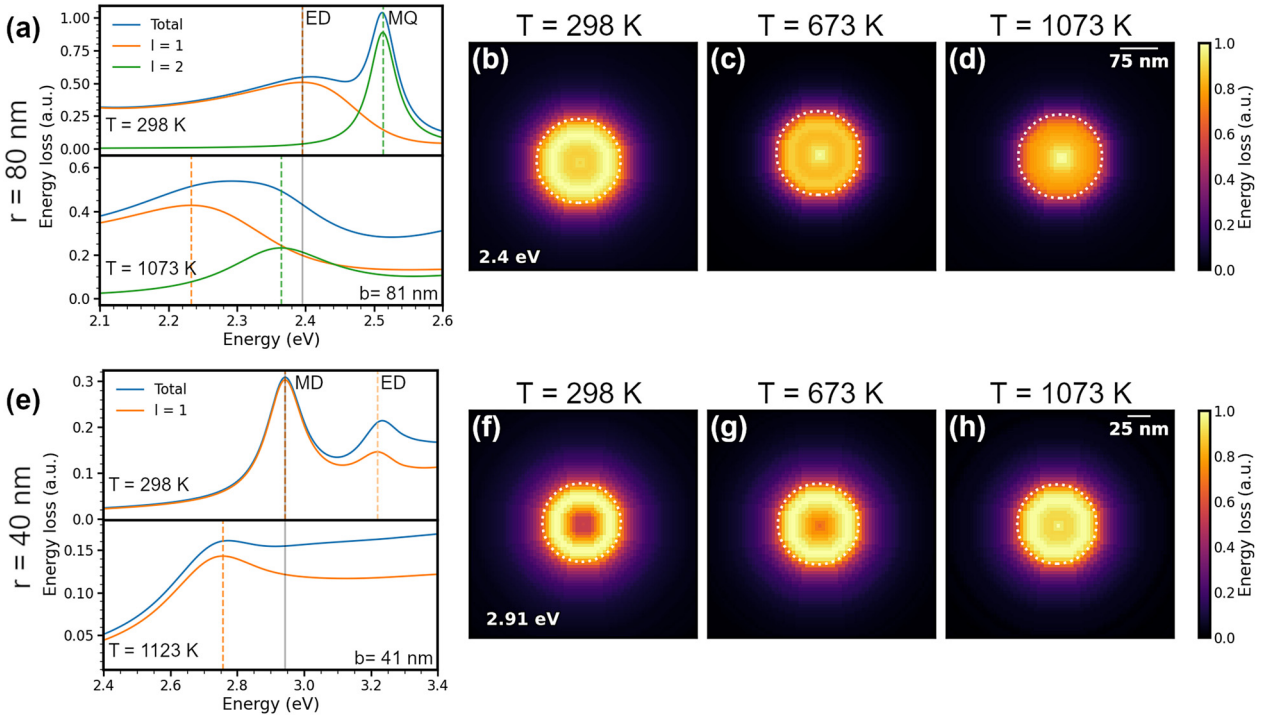

Figure 3: Thermal near-field tuning of silicon Mie modes. (a) Multipole decomposition of the EELS signal into different azimuthal contributions *l* for a particle with $r = 80$ nm. The decomposition is performed at two temperatures for the impact parameter $b = 81$ nm. (b)–(d) Experimental EELS maps of a particle with $r = 82.4 \pm 1.9$ nm for a fixed energy of 2.4 eV (ED at the room temperature) at different temperatures. (e) Multipole EELS decomposition at two temperatures for a particle with $r = 40$ nm with impact parameter $b = 41$ nm. (f)–(h) Experimental EELS maps of a particle with $r = 42.2 \pm 0.7$ nm for a fixed energy of 2.91 eV (MD at the room temperature) at different temperatures.

(Figure 4(e)). Approximately two-thirds of the particles remain stable up to 1073 K, while the remaining particles reshape approximately 100 K below this temperature. This demonstrates that the majority of the particles can be operated at temperatures up to 1073 K without changes in the nanoparticle morphology. To the best of our knowledge, this marks the highest operating temperature of silicon nanoparticles for thermal actuation but is nonetheless smaller than the crystalline silicon melting point (1688 K). Nanoparticles larger than the 40 nm radii range should not display a size-dependent decrease in their melting temperatures [54]. Although the electron beam is also known to induce heating [55], we can safely dismiss this effect as the cause for the reshaping, since particles that were not imaged by the electron beam during the heating also underwent shape changes. We attribute the lower reshaping temperature to the polycrystallinality and doping of our nanoparticles (see Methods). Grain growth in doped polycrystalline silicon starts at relatively low temperatures (below 1173 K) since doping enhances the self-diffusion of silicon [56]. In addition, the highly spherical nature of our nanoparticles entails that crystal planes with high Miller indices are present on the surface, which are known to develop into low-index planes upon heating [57]. Indeed, the reported temperatures for grain growth and reconstruction into low-index planes in silicon (near or above 1073 K) are consistent with the shape and facet changes observed in our experiments.

To demonstrate reversible thermal tuning at such high temperatures, we applied four heating and cooling procedures and recorded the EELS spectra before and after the whole process to detect any changes in the EELS response (Figure 4(f)). As can be seen, the nanoparticle remains stable and the Mie modes are not affected by the multiple heating procedures. This shows that the nanoparticles can be operated in the proposed temperature range up to 1073 K without their operation failure. This is further supported by STEM EDX measurements (see Supplementary Figure S3), where we observe no changes in the chemical composition of the particles when they are heated to 1073 K.

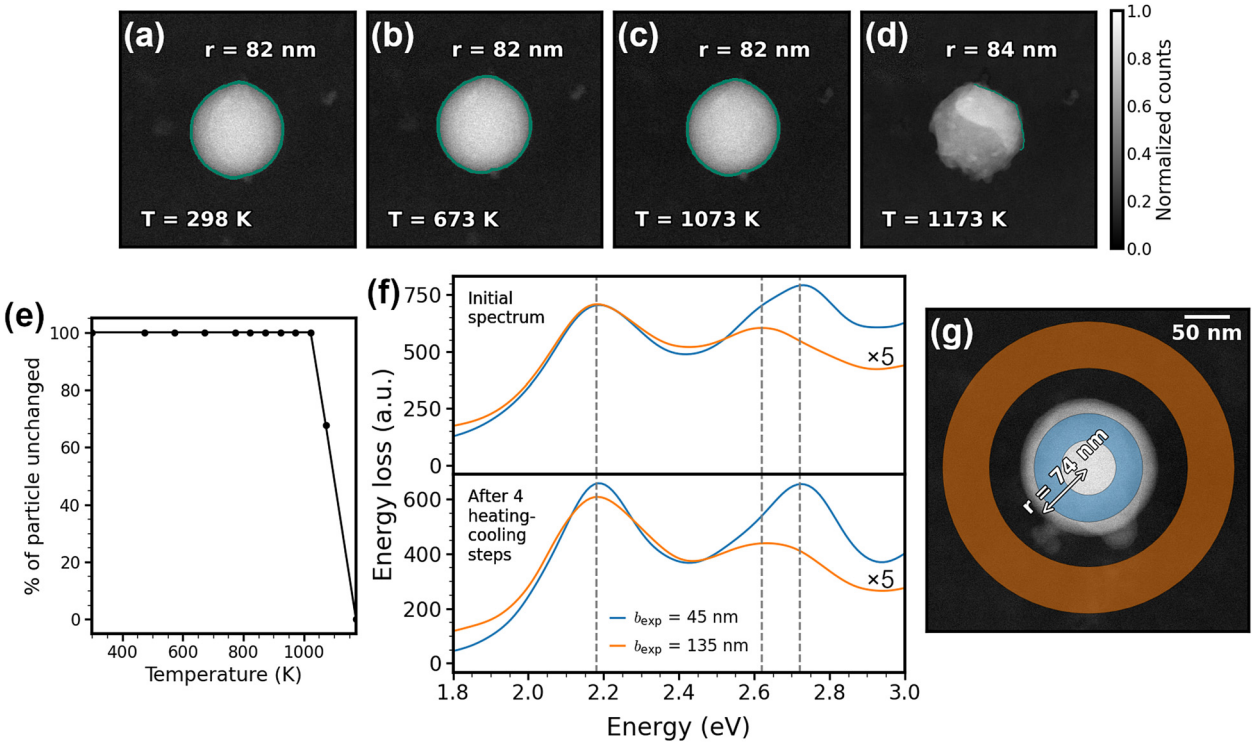

Figure 4: Stability of thermally tuned nanoparticles. (a)–(d) STEM images of a silicon nanoparticle with $r = 82.4 \pm 1.9$ nm at different temperatures. The green selection represents the boundary of the particle. (e) Systematic investigation of morphology changes for 31 different nanoparticles with radii spanning 40–100 nm at elevated temperatures. (f) Experimental EELS spectra of a silicon nanoparticle with a radius $r = 73.8 \pm 2.3$ nm (top) with no heating applied and (bottom) after four heating to 1073 K-cooling to 298 K procedures. The spectra are acquired from the electron beam positions shown in (g). (g) STEM image of the nanoparticle, where the colored areas represent the integration regions for the EELS signal.

3 Conclusions

We have experimentally demonstrated that the Mie modes of silicon nanoparticles in a broad size range can be tuned using the thermo-optic effect. The effect allows tuning the Mie modes of the nanoparticle in the visible spectral range by up 0.15 eV (40 nm). By optimizing the particle size, we show that the MQ mode can be tuned beyond one linewidth, while the MD, ED, and EQ modes offer linewidth tunability ranging from 0.3 to 0.7. The silicon losses at high energies (2.8–3 eV), which ultimately limit further linewidth tunability, can be beneficial for switching applications, i.e., by providing turn on-off functionality.

We leveraged the significant spectral shifts of Mie resonances to demonstrate that near-field profiles of Mie modes can be tuned with temperature and showed that we can effectively switch between two different Mie modes. Despite the lack of spectral peaks for some modes, we still observe significant changes in the near-field profiles. This demonstrates that thermal tuning can be effectively utilized in applications, where the near-field switching between different Mie modes is desired.

By combining *in situ* STEM imaging and EELS, we show there are no significant changes in the spectral response or morphology for the majority of silicon nanoparticles as they are heated to temperatures up to 1073 K, with all particles being stable up to 973 K. Moreover, EDX analysis reveals no chemical changes in the nanoparticle composition. Therefore, the thermal tuning of the Mie resonance with our silicon nanoparticles can be effectively performed up to 1073 K temperature.

4 Methods

4.1 Fabrication

The crystalline silicon nanoparticles of spherical shape are produced by thermal annealing of silicon suboxide (SiO_x) and extraction into methanol [5]. In optical measurement, it has been shown that the scattering spectrum of the nanoparticle perfectly agrees with the Mie theory [58].

A 10 µL solution of silicon nanoparticles in methanol is drop-casted onto commercially available thermal E-chips produced by Protochips, which are nitrogen dried after a 1 min wait time. The chip has a membrane composed of a ceramic layer on top of a 40 nm thick silicon nitride layer. The ceramic layer is used for heating and can be heated up to 1473 K with a temperature accuracy over 95.5% (example: 1073 ± 48 K) and a 99.5% homogeneous temperature profile across the entire chip. It has nine 8 µm holes where only the nitride layer is present. The STEM imaging and EELS characterization is performed in these areas.

4.2 Image analysis

The sizes of the silicon nanoparticles are determined from the STEM images by a previously reported procedure [48]. Using image processing operations with the Python scikit-image library, a canny filter is applied to the STEM image to find the particle edges. A Hough circle transform is applied on the edge map to find the best fit for the radius and particle center. The uncertainty in the radius is determined by fitting the number of intersections-radius dependence with a bimodal distribution of 2 Gaussians.

4.3 EELS measurements and analysis

The EELS measurements are performed in a monochromated and aberration-corrected FEI Titan operated in STEM mode at an acceleration voltage of 300 kV, providing a probe size of ∼ 0.5 nm and an energy resolution of 0.08 eV (as measured by the full-width-at-half-maximum of the zero-loss peak). We perform Richardson–Lucy deconvolution to remove the zero-loss peak. An EELS spectrum obtained in a vacuum is used as an input for the point-spread function. Due to a small asymmetry in the zero-loss peak, the deconvolution algorithm produced an artificial EELS peak in the energy range below 0.6 eV. However, the artificial peak did not overlap with any of the observed resonances and could be safely removed using a first-order logarithmic polynomial.

The depicted EELS spectra are obtained by integrating the deconvoluted EELS data around the experimental impact parameter b_{exp}. For the disk-shaped integration regions, the experimental impact parameter denotes the center of the disk. For the annulus-shaped regions, the experimental impact parameter denotes the mean of the inner and outer radii. The depicted EELS spectra are smoothed with a Gaussian function ($\sigma = 0.03$ eV).

The EELS maps are obtained by summing the deconvoluted EELS data in a spectral window of 0.02 eV width centered at the resonance energies. To improve the signal-to-noise ratio, the map is spatially binned, reducing the effective number of pixels by a factor of 2 in each row and column, i.e., a factor of 4 in total. A Gaussian filter with $\sigma = 0.8$ pixels is applied to smooth the image. Exploiting the spherical symmetry of the nanoparticles, the maps are integrated along the azimuth angle at the coordinates located at the same distance from the nanoparticle center.

4.4 EELS simulations and theory

The EELS simulations are performed in COMSOL Multiphysics, which solves Maxwell's equations using finite-element modeling. We simulate the electron beam as an edge current with an amplitude of 1 µA. The induced electromagnetic field is determined by calculating the fields with and without the silicon nanoparticle in the simulation domain, and subsequently subtracting them. Using the obtained induced electric field, the energy loss can be calculated as the work rate done on the electron beam by the electromagnetic field induced by the optical structure [59]. The temperature-dependent complex refractive index for silicon is taken from Reference [51]. The silicon nitride layer is not included in the simulation since it has negligible influence on the optical properties of Mie resonances throughout the visible spectral range [48].

The multipole decomposition of the EELS spectra is obtained via a multipole expansion of the electromagnetic field produced by an electron exciting a dielectric sphere in a vacuum [53]. The refractive index data is taken from Reference [51], while in Figure 3(e) it is taken from Reference [60]. This is due to a limited energy range of the refractive index data in the former case.

The linewidth tunability $\Delta\lambda/\mathrm{FWHM}$ of Mie resonances in Figure 2 is calculated from the theoretical EELS spectra of a sphere at a fixed impact parameter $b = 2r$. The theoretical EELS spectra are calculated for separate azimuthal coefficients $l = 1, 2$. Then, they are fitted with two Lorentzian functions, resulting in the parameters for different couples of multipoles (MD and ED for $l = 1$, MQ and EQ for $l = 2$). The resonance wavelength is fixed and is defined as the first maxima of the Mie scattering coefficient for a respective multipole, and the full-width at half-maximum of the Lorentzian is found from the fit. A split Lorentzian function (width of the distribution is different between left and right slopes) is used for the ED mode, while a symmetrical Lorentzian function is used for the rest of the modes. The fit is performed using the python package LMFIT.

Author contribution: S. R. conceived the experiments and supervised the project. A. A. fabricated the samples, performed the EELS measurements, the image and EELS data analyses, the simulations. T. H., H. S., and M. J. fabricated the silicon nanoparticles. A. A. and S. R. prepared figures and wrote the manuscript. All authors discussed the results and contributed to the preparation of the manuscript.

Research funding: S. R. and A. A. acknowledge support by the Independent Research Funding Denmark (7026-00117B).

Conflict of interest statement: The authors declare no competing financial interests.

Data and materials availability: All data needed to evaluate the conclusions in the paper are present in the paper and/or the Supplementary Materials. Additional data related to this paper may be requested from the corresponding author.

References

[1] A. I. Kuznetsov, A. E. Miroshnichenko, M. L. Brongersma, Y. S. Kivshar, and B. Luk'yanchuk, "Optically resonant dielectric nanostructures," *Science*, vol. 354, p. aag2472, 2016.

[2] A. E. Krasnok, A. E. Miroshnichenko, P. A. Belov, and Y. S. Kivshar, "All-dielectric optical nanoantennas," *Opt. Express*, vol. 20, pp. 20599–20604, 2012.

[3] A. E. Krasnok, C. R. Simovski, P. A. Belov, and Y. S. Kivshar, "Superdirective dielectric nanoantennas," *Nanoscale*, vol. 6, pp. 7354–7361, 2014.
[4] T. Feng, W. Zhang, Z. Liang, and Y. Xu, "Unidirectional emission in an all-dielectric nanoantenna," *J. Phys. Condens. Matter*, vol. 30, p. 124002, 2018.
[5] H. Sugimoto and M. Fujii, "Colloidal dispersion of subquarter micrometer silicon spheres for low-loss antenna in visible regime," *Adv. Opt. Mater.*, vol. 5, p. 1700332, 2017.
[6] M. R. Shcherbakov, D. N. Neshev, B. Hopkins, et al., "Enhanced third-harmonic generation in silicon nanoparticles driven by magnetic response," *Nano Lett.*, vol. 14, pp. 6488–6492, 2014.
[7] D. Smirnova, A. I. Smirnov, and Y. S. Kivshar, "Multipolar second-harmonic generation by Mie-resonant dielectric nanoparticles," *Phys. Rev. A*, vol. 97, p. 013807, 2018.
[8] K. Koshelev, S. Kruk, E. Melik-Gaykazyan, et al., "Subwavelength dielectric resonators for nonlinear nanophotonics," *Science*, vol. 367, pp. 288–292, 2020.
[9] P. Moitra, B. A. Slovick, W. li, et al., "Large-scale all-dielectric metamaterial perfect reflectors," *ACS Photonics*, vol. 2, pp. 692–698, 2015.
[10] A. Arbabi, Y. Horie, M. Bagheri, and A. Faraon, "Dielectric metasurfaces for complete control of phase and polarization with subwavelength spatial resolution and high transmission," *Nat. Nanotechnol.*, vol. 10, pp. 937–943, 2015.
[11] M. Khorasaninejad, W. T. Chen, R. C. Devlin, J. Oh, A. Y. Zhu, and F. Capasso, "Metalenses at visible wavelengths: diffraction-limited focusing and subwavelength resolution imaging," *Science*, vol. 352, pp. 1190–1194, 2016.
[12] A. Vaskin, S. Mashhadi, M. Steinert, et al., "Manipulation of magnetic dipole emission from Eu^{3+} with Mie-resonant dielectric metasurfaces," *Nano Lett.*, vol. 19, pp. 1015–1022, 2019.
[13] A. M. Shaltout, V. M. Shalaev, and M. L. Brongersma, "Spatiotemporal light control with active metasurfaces," *Science*, vol. 364, p. eaat3100, 2019.
[14] C. Zou, J. Sautter, F. Setzpfandt, and I. Staude, "Resonant dielectric metasurfaces: active tuning and nonlinear effects," *J. Phys. D Appl. Phys.*, vol. 52, p. 373002, 2019.
[15] G. P. Zograf, M. I. Petrov, D. A. Zuev, et al., "Resonant nonplasmonic nanoparticles for efficient temperature-feedback optical heating," *Nano Lett.*, vol. 17, pp. 2945–2952, 2017.
[16] T. Zhang, Y. Che, K. Chen, et al., "Anapole mediated giant photothermal nonlinearity in nanostructured silicon," *Nat. Commun.*, vol. 11, p. 3027, 2020.
[17] P. Gutruf, C. Zou, W. Withayachumnankul, M. Bhaskaran, S. Sriram, and C. Fumeaux, "Mechanically tunable dielectric resonator metasurfaces at visible frequencies," *ACS Nano*, vol. 10, pp. 133–141, 2015.
[18] A. L. Holsteen, S. Raza, P. Fan, P. G. Kik, and M. L. Brongersma, "Purcell effect for active tuning of light scattering from semiconductor optical antennas," *Science*, vol. 358, pp. 1407–1410, 2017.
[19] K. Lee, J. Son, J. Park, et al., "Linear frequency conversion via sudden merging of meta-atoms in time-variant metasurfaces," *Nat. Photonics*, vol. 12, pp. 765–773, 2018.
[20] J. Xiang, J. Chen, Q. Dai, S. Tie, S. Lan, and A. E. Miroshnichenko, "Modifying Mie resonances and carrier dynamics of silicon nanoparticles by dense electron-hole plasmas," *Phys. Rev. Appl.*, vol. 13, p. 014003, 2020.
[21] J. Sautter, I. Staude, M. Decker, et al., "Active tuning of all-dielectric metasurfaces," *ACS Nano*, vol. 9, pp. 4308–4315, 2015.
[22] M. Parry, A. Komar, B. Hopkins, et al., "Active tuning of high-Q dielectric metasurfaces," *Appl. Phys. Lett.*, vol. 111, p. 053102, 2017.
[23] S. Q. Li, X. Xu, R. Maruthiyodan Veetil, V. Valuckas, R. Paniagua-Domínguez, and A. I. Kuznetsov, "Phase-only transmissive spatial light modulator based on tunable dielectric metasurface," *Science*, vol. 364, pp. 1087–1090, 2019.
[24] Q. Wang, E. T. F. Rogers, B. Gholipour, et al., "Optically reconfigurable metasurfaces and photonic devices based on phase change materials," *Nat. Photonics*, vol. 10, pp. 60–65, 2016.
[25] J. Tian, H. Luo, Y. Yang, et al., "Active control of anapole states by structuring the phase-change alloy $Ge_2Sb_2Te_5$," *Nat. Commun.*, vol. 10, p. 396, 2019.
[26] Y. Zhang, C. Fowler, J. Liang, et al., "Electrically reconfigurable non-volatile metasurface using low-loss optical phase-change material," *Nat. Nanotechnol.*, vol. 16, pp. 661–666, 2021.
[27] T. Lewi, H. A. Evans, N. A. Butakov, and J. A. Schuller, "Ultrawide thermo-optic tuning of PbTe meta-atoms," *Nano Lett.*, vol. 17, pp. 3940–3945, 2017.
[28] P. Berto, L. Philippet, J. Osmond, et al., "Tunable and free-form planar optics," *Nat. Photonics*, vol. 13, pp. 649–656, 2019.
[29] M. Rahmani, L. Xu, A. E. Miroshnichenko, et al., "Reversible thermal tuning of all-dielectric metasurfaces," *Adv. Funct. Mater.*, vol. 27, p. 1700580, 2017.
[30] T. Lewi, N. A. Butakov, and J. A. Schuller, "Thermal tuning capabilities of semiconductor metasurface resonators," *Nanophotonics*, vol. 8, pp. 331–338, 2019.
[31] T. Lewi, N. A. Butakov, H. A. Evans, et al., "Thermally reconfigurable meta-optics," *IEEE Photon. J.*, vol. 11, pp. 1–16, 2019.
[32] K. Z. Kamali, L. Xu, J. Ward, et al., "Reversible image contrast manipulation with thermally tunable dielectric metasurfaces," *Small*, vol. 15, p. 1805142, 2019.
[33] J. Ward, K. Zangeneh Kamali, L. Xu, G. Zhang, A. E. Miroshnichenko, and M. Rahmani, "High-contrast and reversible scattering switching via hybrid metal-dielectric metasurfaces," *Beilstein J. Nanotechnol.*, vol. 9, pp. 460–467, 2018.
[34] G. Grinblat, H. Zhang, M. P. Nielsen, et al., "Efficient ultrafast all-optical modulation in a nonlinear crystalline gallium phosphide nanodisk at the anapole excitation," *Sci. Adv.*, vol. 6, p. eabb3123, 2020.
[35] M. Caldarola, P. Albella, E. Cortés, et al., "Non-plasmonic nanoantennas for surface enhanced spectroscopies with ultra-low heat conversion," *Nat. Commun.*, vol. 6, p. 7915, 2015.
[36] D. G. Baranov, R. Verre, P. Karpinski, and M. Käll, "Anapole-enhanced intrinsic Raman scattering from silicon nanodisks," *ACS Photonics*, vol. 5, pp. 2730–2736, 2018.

[37] S. Raza and A. Kristensen, "Raman scattering in high-refractive-index nanostructures," *Nanophotonics*, vol. 10, pp. 1197–1209, 2021.
[38] A. F. Cihan, A. G. Curto, S. Raza, P. G. Kik, and M. L. Brongersma, "Silicon Mie resonators for highly directional light emission from monolayer MoS_2," *Nat. Photonics*, vol. 12, pp. 284–290, 2018.
[39] S. Liu, A. Vaskin, S. Addamane, et al., "Light-emitting metasurfaces: simultaneous control of spontaneous emission and far-field radiation," *Nano Lett.*, vol. 18, pp. 6906–6914, 2018.
[40] A. Vaskin, J. Bohn, K. E. Chong, et al., "Directional and spectral shaping of light emission with Mie-resonant silicon nanoantenna arrays," *ACS Photonics*, vol. 5, pp. 1359–1364, 2018.
[41] R. F. Egerton, "Electron energy-loss spectroscopy in the TEM," *Rep. Prog. Phys.*, vol. 72, p. 016502, 2009.
[42] F. J. García de Abajo, "Optical excitations in electron microscopy," *Rev. Mod. Phys.*, vol. 82, pp. 210–256, 2010.
[43] C. Colliex, M. Kociak, and O. Stéphan, "Electron energy loss spectroscopy imaging of surface plasmons at the nanometer scale," *Ultramicroscopy*, vol. 162, pp. A1–A24, 2016.
[44] S. Raza, M. Esfandyarpour, A. L. Koh, N. A. Mortensen, M. L. Brongersma, and S. I. Bozhevolnyi, "Electron energy-loss spectroscopy of branched gap plasmon resonators," *Nat. Commun.*, vol. 7, p. 13790, 2016.
[45] E. P. Bellido, G. D. Bernasconi, D. Rossouw, J. Butet, O. J. F. Martin, and G. A. Botton, "Self-similarity of plasmon edge modes on Koch fractal antennas," *ACS Nano*, vol. 11, pp. 11240–11249, 2017.
[46] V. Flauraud, G. D. Bernasconi, J. Butet, D. T. L. Alexander, O. J. F. Martin, and J. Brugger, "Mode coupling in plasmonic heterodimers probed with electron energy loss spectroscopy," *ACS Nano*, vol. 11, pp. 3485–3495, 2017.
[47] D. Kordahl, D. T. Alexander, and C. Dwyer, "Waveguide modes spatially resolved by low-loss STEM-EELS," *Phys. Rev. B*, vol. 103, p. 134109, 2021.
[48] A. Assadillayev, T. Hinamoto, M. Fujii, H. Sugimoto, M. L. Brongersma, and S. Raza, "Plasmon launching and scattering by silicon nanoparticles," *ACS Photonics*, vol. 8, p. 48, 2021.
[49] J. H. Song, S. Raza, J. van de Groep, et al., "Nanoelectromechanical modulation of a strongly-coupled plasmonic dimer," *Nat. Commun.*, vol. 12, p. 48, 2021.
[50] P. Lautenschlager, M. Garriga, L. Vina, and M. Cardona, "Temperature dependence of the dielectric function and interband critical points in silicon," *Phys. Rev. B*, vol. 36, p. 4821, 1987.
[51] G. E. Jellison, J. Modine, and F. A. Modine, "Optical functions of silicon at elevated temperatures," *J. Appl. Phys.*, vol. 76, pp. 3758–3761, 1994.
[52] G. E. Jellison, Jr and F. A. Modine, "Optical absorption of silicon between 1.6 and 4.7 eV at elevated temperatures," *Appl. Phys. Lett.*, vol. 41, p. 180, 1982.
[53] F. J. García de Abajo, "Relativistic energy loss and induced photon emission in the interaction of a dielectric sphere with an external electron beam," *Phys. Rev. B*, vol. 59, pp. 3095–3107, 1999.
[54] I. V. Talyzin, M. V. Samsonov, V. M. Samsonov, M. Y. Pushkar, and V. V. Dronnikov, "Size dependence of the melting point of silicon nanoparticles: molecular dynamics and thermodynamic simulation," *Semiconductors*, vol. 53, pp. 947–953, 2019.
[55] M. A. Asoro, D. Kovar, and P. J. Ferreira, "In situ transmission electron microscopy observations of sublimation in silver nanoparticles," *ACS Nano*, vol. 7, pp. 7844–7852, 2013.
[56] Y. Wada and S. Nishimatsu, "Grain growth mechanism of heavily phosphorus-implanted polycrystalline silicon," *J. Electrochem. Soc.*, vol. 125, p. 1499, 1978.
[57] T. Tsong, D. Feng, and H. Liu, "Atomic structures in reconstruction of high index surfaces of silicon," *Surf. Sci.*, vol. 199, pp. 421–438, 1988.
[58] H. Sugimoto, T. Hinamoto, and M. Fujii, "Forward to backward scattering ratio of dielectric–metal heterodimer suspended in almost free-space," *Adv. Opt. Mater.*, vol. 7, p. 1900591, 2019.
[59] A. L. Koh, A. I. Fernández-Domínguez, D. W. McComb, S. A. Maier, and J. K. W. Yang, "High-resolution mapping of electron-beam-excited plasmon modes in lithographically defined gold nanostructures," *Nano Lett.*, vol. 11, pp. 1323–1330, 2011.
[60] J. Šik, J. Hora, and J. Humlíček, "Optical functions of silicon at high temperatures," *J. Appl. Phys.*, vol. 84, pp. 6291–6298, 1998.

Supplementary Material: The online version of this article offers supplementary material (https://doi.org/10.1515/nanoph-2021-0424).